Chemical Science

ROYAL SOCIETY OF CHEMISTRY

EDGE ARTICLE

View Article Online
View Journal | View Issue

Cite this: *Chem. Sci.*, 2025, **16**, 13905

All publication charges for this article have been paid for by the Royal Society of Chemistry

Stable and highly selective Co-CeF_3@Ni_3N sheet-on-sheet heterostructures for PET electro-upgrading and hydrogen production†

Kuan Deng,[a] Xuesong Liu,[a] Peng Liu,[a] Xingbin Lv,[b] Wen Tian[a] and Junyi Ji *[a]

The electro-upgrading of polyethylene terephthalate (PET) alkaline hydrolysate provides an energy-saving strategy towards green hydrogen and value-added anodic products, but the selectivity and stability at industrial-scale current densities (>200 mA cm^{-2}) remain challenging. Herein, hierarchical Co-CeF_3@Ni_3N sheet-on-sheet nanostructures supported on nickel foam (Co-CeF_3@Ni_3N/NF) were fabricated for PET hydrolysate electro-upgrading coupled with H_2 generation. The hierarchical nanostructures can enlarge the accessible active area, while the introduction of Co species can modulate the electronic configuration, which can reduce the active species formation potential and optimize the adsorption behaviors of key reactants and reactive intermediates. Therefore, Co-CeF_3@Ni_3N/NF exhibits industrial-scale response current densities (80 to 380 mA cm^{-2}) at applied potentials of around 1.32–1.44 V *vs.* RHE, as well as high stability (over 60 h) and high faradaic efficiencies (>97%) in the ethylene glycol oxidation reaction (EGOR), which are superior to most high-end electrocatalysts. *In situ* characterizations and electrochemical measurements indicate the key active species and crucial intermediates in the EGOR, suggesting a reaction pathway towards high formate selectivity. Moreover, a continuous flow cell with Co-CeF_3@Ni_3N/NF as the bifunctional electrode for electro-upgrading PET hydrolysate delivers high activity (over 300 mA cm^{-2} at 1.72 V), long-term stability (144 h) and high FEs (>95%). This study develops a bifunctional electrocatalyst for the EGOR and HER, while elucidating the active species, key intermediates, and possible reaction pathway for the closed-loop electro-upgrading of PET waste.

Received 11th April 2025
Accepted 22nd June 2025

DOI: 10.1039/d5sc02685g

rsc.li/chemical-science

Introduction

Polyethylene terephthalate (PET) is a thermoplastic polymer widely used for various consumer products due to its high transparency, light weight, and good chemical stability.[1,2] However, the wide-spread of degradation-resistant PET products (70 million tons per year) has led to the substantial accumulation of PET plastic waste, contributing to the issue of "white pollution" with serious environmental challenges.[3–6] Therefore, the efficient disposal of vast quantities of waste PET is an urgent social and scientific challenge. Recycling is a vital strategy for managing waste PET plastics and reducing their environmental impact.[7] Currently, 90% of PET recycling is carried out through mechanical recycling, but the quality of the recycled PET may degrade with each cycle, while the removal of contaminants is also challenging.[8] In addition, waste PET can be hydrolyzed to produce terephthalic acid (TPA) and ethylene glycol (EG) monomers by chemical recycling under alkaline conditions.[9] Afterward, adjusting the pH of PET hydrolysate can facilitate the precipitation and separation of TPA, but the EG is hard to separate due to its good water solubility and high boiling point.[10,11] Therefore, to achieve the efficient recycling of PET plastics, there is an urgent need to explore efficient and sustainable treatment processes that enable the closed-loop recycling of TPA from waste PET plastics and the conversion of EG into high-value-added and easy-separation products.[12–14]

Recently, collaborative electrocatalytic systems combining small organic molecule oxidation reactions with the hydrogen evolution reaction (HER) have garnered widespread attention due to their low energy consumption and generation of value-added products on the anode side.[15–17] Therein, the development of the ethylene glycol oxidation reaction (EGOR) provides a reliable and effective upcycling route for the recycling of PET. Generally, EG molecules can be transformed to value-added products by the direct electrooxidation of the alkaline PET hydrolysate without purification or the addition of extra chemicals. However, due to the existence of two hydroxyl groups and a C–C bond in EG, the main products obtained from the

[a]*School of Chemical Engineering, State Key Laboratory of Polymer Materials Engineering, Sichuan University, Chengdu 610065, P. R. China. E-mail: junyiji@scu.edu.cn*

[b]*College of Chemistry and Environment, Southwest Minzu University, Chengdu, Sichuan 610041, P. R. China*

† Electronic supplementary information (ESI) available. See DOI: https://doi.org/10.1039/d5sc02685g

EGOR are various C_1 or C_2 chemicals, such as formic acid (FA), glycolic acid (GA), and oxalic acid (OA).[18–20] Among the various potential electrooxidation reaction pathways and products, controlling the reaction selectivity is a key issue in the design and development of EGOR electrocatalysts, which can not only improve the reaction stability but also facilitate subsequent product separation processes. Therefore, the design of electrocatalysts with high EGOR activity, stability and selectivity remains challenging, especially at industrial-scale current densities (>200 mA cm^{-2}).[21] Although noble-metal-based electrocatalysts, such Pd, Pt, and Au, exhibit high catalytic performance, their high cost, inferior long-term stability and variety of by-products limit their practical applications.[22–24] Currently, related alternative transition-metal-based electrocatalysts have been developed for the EGOR,[25,26] but they still suffer from various side reactions, leading to inferior faradaic efficiencies. Therefore, the rational design of transition-metal-based electrocatalysts to boost the activity and selectivity is of great significance.[27]

To design EGOR electrocatalysts with superior selectivity, it is crucial to elucidate the reaction pathway and identify the key intermediates of the EGOR. The electrooxidation pathways of EG predominantly involve two distinct oxidative mechanisms, the oxidation of hydroxyl groups and/or the cleavage of C–C bonds.[28,29] The sequencing of these two kinds of oxidations and the oxidation depth of hydroxyl groups lead to the differences in intermediates and reaction pathways, further resulting in a diversity of final electrooxidation products. Meanwhile, the adsorption capacity for organic intermediates and OH^- can be effectively regulated by modulating the surface electronic configuration and geometric structure, thereby influencing the product selectivity of the EGOR.[30,31] In previous studies, glycolate or glyoxal are usually determined as the key intermediates for the EGOR on Ni-based electrocatalysts.[32,33] Although both intermediates can be further transformed to formate, the divergent reaction pathways may induce distinct product selectivity. Therefore, rational electrode design to create specific active sites for EGOR process, coupled with strategies to modulate the interface adsorption and transformation efficiency of reactants/intermediates to steer reaction pathways also need to be developed.

In the anodic oxidation process, cobalt-based species have been demonstrated to facilitate the adsorption of OH^-.[34,35] Therefore, hierarchical Co-CeF_3@Ni_3N sheet-on-sheet nanostructures supported on nickel foam (Co-CeF_3@Ni_3N/NF) were fabricated as a bifunctional electrocatalyst for the electro-upgrading of PET hydrolysate to added-value chemicals, coupled with H_2 generation. The hierarchical sheet-on-sheet nanostructures can expand the accessible surface area and the coating of Co species can reduce the onset oxidation potential for the EGOR. Therefore, the Co-CeF_3@Ni_3N/NF electrode exhibits industrial-scale current densities, high stability (over 60 h) and high FEs (>97%) at 1.32–1.44 V *vs.* RHE in the EGOR. Furthermore, a continuous flow cell with Co-CeF_3@Ni_3N/NF as the bifunctional electrode in an electro-upgrading PET hydrolysate system delivers 100/300 mA cm^{-2} at 1.50/1.72 V, and it can remain stable at 1.75 V over 6 cycles for 144 h. Moreover, *operando* electrochemical impedance spectroscopy and *in situ* Raman spectroscopy were implemented to track the dynamic evolution of active species during the EGOR. *In situ* Fourier transform infrared spectroscopy and a series of electrochemical measurements indicated that glyoxal is a crucial intermediate in the EGOR using the Co-CeF_3@Ni_3N/NF electrocatalyst, while a possible reaction pathway is also proposed.

Results and discussion

As shown in Fig. 1a, the CeF_3@Ni_3N heterostructure supported on Ni foam (CeF_3@Ni_3N/NF) is fabricated following our previous work.[36] Afterward, CeF_3@Ni_3N/NF is immersed in $Co(Ac)_2$ solution to spontaneously fabricate hierarchical Co-CeF_3@Ni_3N nanosheet arrays on NF (Co-CeF_3@Ni_3N/NF) through an interfacial reaction. The morphological features are investigated using scanning electron microscopy (SEM). Typically, vertically aligned nanosheet arrays can be observed in F-$Ni(OH)_2$/NF, NiCeF precursor/NF, and CeF_3@Ni_3N/NF (Fig. S1†). Meanwhile, the X-ray diffraction (XRD) spectra indicate the distinct crystalline change after the introduction of Ce species (Fig. S2†), demonstrating the successful fabrication of CeF_3@Ni_3N heterostructures on the NF substrate. After spontaneous coating with Co species, the Co-CeF_3@Ni_3N/NF composite reveals distinct hierarchical sheet-on-sheet nanostructures (Fig. 1b, c and S3†), where small nanosheets with a lateral size of about 150 nm are vertically and uniformly anchored on CeF_3@Ni_3N nanosheets to enlarge the accessible active surface area. Moreover, energy dispersive spectroscopy (EDS) mapping reveals the uniform distribution of Co, Ni, Ce, F, N, and O elements (Fig. S4†), further confirming the successful introduction of Co species to form sheet-on-sheet nanostructures without structural collapse. As illustrated in the XRD patterns (Fig. 1d), diffraction peaks in the pattern of CeF_3@Ni_3N/NF corresponding to the Ni_3N phase (JCPDS 10-0280) and CeF_3 phase (JCPDS 08-0045) can be observed, indicating the formation of CeF_3@Ni_3N heterostructures with high crystallinity.[36–38] For Co-CeF_3@Ni_3N/NF, no new phases can be detected, indicating the amorphous nature of the newly introduced Co species. Furthermore, the hierarchical sheet-on-sheet nanostructures of Co-CeF_3@Ni_3N are also confirmed using transmission electron microscopy (TEM). As shown in Fig. 1e, a large number of vertically aligned ultrasmall nanosheets are present on the large sheet surface. Moreover, the crystalline spacing values of 0.21 and 0.20 nm correspond to the (002) and (111) planes of Ni_3N, respectively, while that of 0.32 nm is related to the (111) plane of CeF_3 (Fig. 1f and g). The selective area electron diffraction (SAED) pattern of Co-CeF_3@Ni_3N exhibits distinct diffraction rings that arise from the main lattice planes of Ni_3N and CeF_3 (inset of Fig. 1e), which is in line with the XRD results. In Fig. 1h, high-angle annular dark-field scanning transmission electron microscopy (HAADF-STEM) imaging and related EDX mapping reveal the homogeneous distribution of Ce, Co, Ni, F, N, and O elements on the Co-CeF_3@Ni_3N nanosheets, demonstrating the uniform and dense anchoring of ultrasmall Co-based nanosheets.

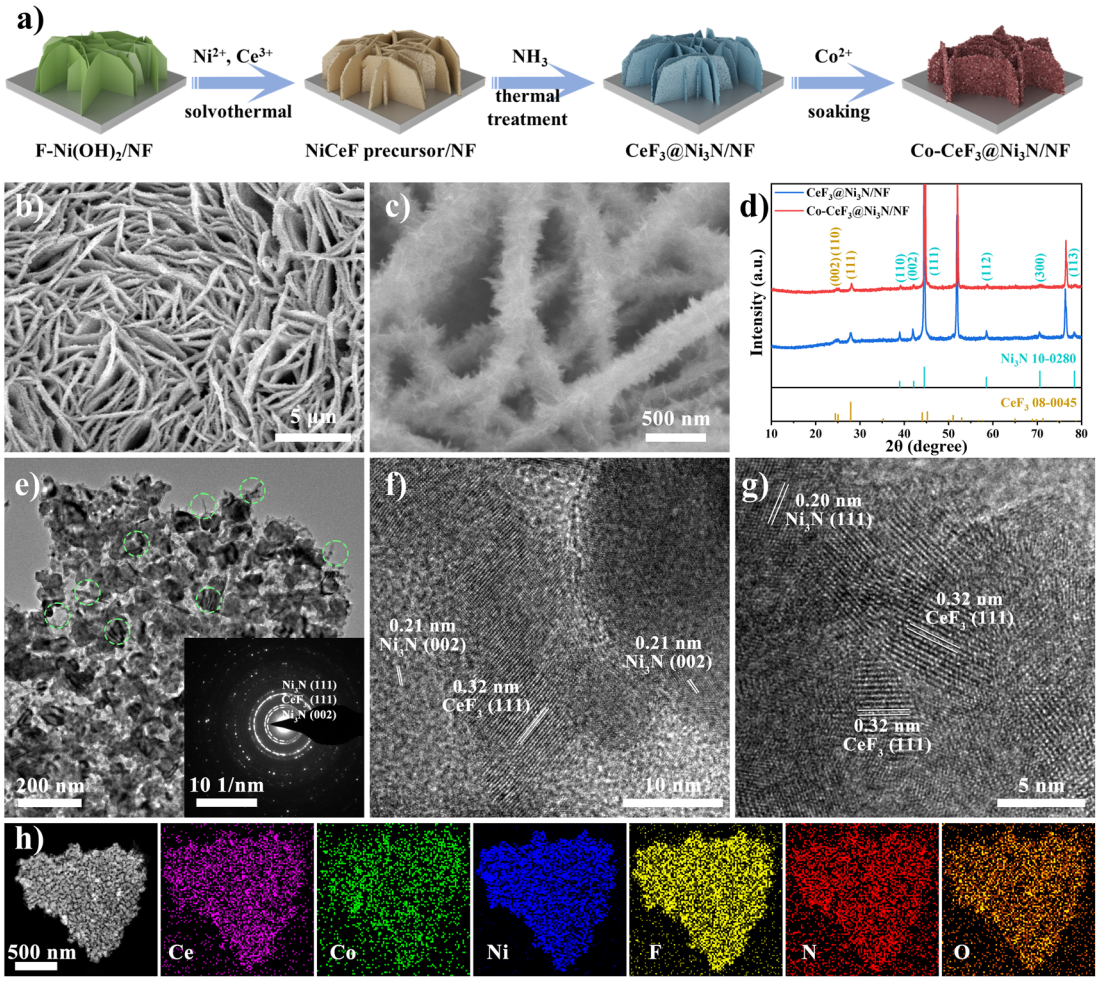

Fig. 1 (a) A schematic illustration of the synthetic procedure for Co-CeF_3@Ni_3N/NF. (b) and (c) SEM images of Co-CeF_3@Ni_3N/NF. (d) XRD patterns of CeF_3@Ni_3N/NF and Co-CeF_3@Ni_3N/NF. (e)–(g) TEM images and the SAED pattern of Co-CeF_3@Ni_3N. (h) A HAADF-STEM image and corresponding EDX mapping of Co-CeF_3@Ni_3N.

X-ray photoelectron spectroscopy (XPS) is utilized to confirm the elemental chemical valence states and electronic interactions of Co-CeF_3@Ni_3N/NF and CeF_3@Ni_3N/NF. The full survey of Co-CeF_3@Ni_3N/NF clearly demonstrates the presence of C, Co, Ni, Ce, N, F, and O elements (Fig. S5†), confirming the successful incorporation of Co species. In the C 1s spectrum, three peaks located at 284.8, 286.7, and 289.2 eV can be assigned to C–C/C=C, C–O/C–N, and O=C–O (Fig. 2a), respectively.[39] As shown in Fig. 2b, the Ni $2p_{3/2}$ spectrum exhibits three typical peaks centred at 853.9, 856.0, and 861.0 eV, which are assigned to Ni^+ within the nitride lattice (Ni–N), surface-oxidized Ni^{2+} (Ni–O), and a shake-up satellite peak, respectively.[40,41] In the deconvoluted Ce 3d spectra of Co-CeF_3@Ni_3N/NF and CeF_3@Ni_3N/NF (Fig. 2c and Table S1†), the Ce $3d_{5/2}$ and Ce $3d_{3/2}$ peaks are marked as u and v peaks, respectively. The two peaks labeled as u′ and v′ correspond to Ce^{3+} species, while the other six peaks are associated with the +4 valence state.[42,43] The coexistence of Ce^{3+} and Ce^{4+} species is attributed to the flexible Ce^{3+}/Ce^{4+} redox transition nature of CeF_3, which is beneficial for modulating the surface adsorption capabilities. Moreover, the $Ce^{4+}/(Ce^{3+} + Ce^{4+})$ ratio in Co-CeF_3@Ni_3N/NF (66.16%) is lower than that in CeF_3@Ni_3N/NF (74.85%), indicating the increase in vacancy sites on the electrode surface. The Co 2p spectrum of Co-CeF_3@Ni_3N/NF displays two peaks located at 781.0 and 796.1 eV corresponding to Co^{2+} species, along with two satellite peaks centred at 785.8 and 801.5 eV (Fig. 2d).[44–46] In addition, the N 1s spectrum reveals a single peak centred at 398.9 eV related to the Ni–N bond (Fig. 2e),[47] while the F 1s spectrum shows a characteristic peak located at 684.8 eV for the Ce–F bond (Fig. 2f).[48] Moreover, upon the introduction of Co species, the binding energy of the Ni–N band in Ni 2p experiences a positive shift of approximately 0.3 eV relative to that of CeF_3@Ni_3N/NF, while the binding energies of Ce^{3+} and Ce^{4+} also experience a negative shift of 0.3 eV, which may due to enhanced interfacial electronic interactions and electron transfer capabilities between Ni_3N and CeF_3 heterogeneous interfaces under the influence of Co species. The above results demonstrated that the rational construction of Co-CeF_3@Ni_3N/NF sheet-on-sheet heterostructures not only increases the oxidation state of Ni_3N, but

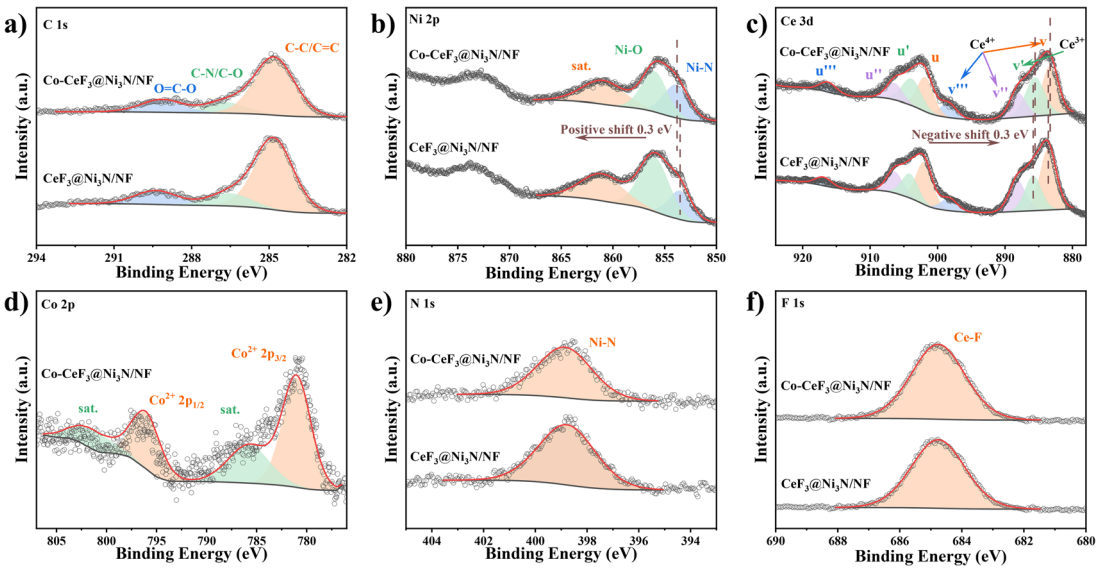

Fig. 2 (a) C 1s, (b) Ni 2p, (c) Ce 3d, (d) Co 2p, (e) N 1s, and (f) F 1s XPS spectra of Co-CeF_3@Ni_3N/NF and CeF_3@Ni_3N/NF.

also simultaneously modulates the surface electronic configuration *via* Co species coating. Apparently, synergistic interfacial electronic engineering may optimize the adsorption behaviours of key reactants and reactive intermediates, significantly enhancing the electrocatalytic activity and selectivity *via* improved reaction selectivity.[49]

The electrochemical performance of the as-prepared composites for the OER and EGOR was assessed in a standard three-electrode H-type electrolyzer without an ion-exchange membrane. Firstly, cyclic voltammetry (CV) curves were obtained in 1 M KOH solution to investigate the surface redox tendencies of various electrodes (Fig. 3a). Compared to CeF_3@Ni_3N/NF, the anodic peak corresponding to the Ni^{2+}/Ni^{3+} redox couple in Co-CeF_3@Ni_3N/NF is negatively shifted and significantly enhanced, suggesting that the introduction of Co species can modulate the electronic configuration around Ni atoms and facilitate the surface adsorption of OH^-, thereby promoting the formation of $Ni^{3+}OOH$ species.[50] Moreover, a series of linear sweep voltammetry (LSV) curves for Co-CeF_3@Ni_3N/NF was obtained at various EG concentrations to investigate the effect on the EGOR process and to determine the optimal EG concentration. The response current density of the EGOR using Co-CeF_3@Ni_3N/NF gradually increases until the EG concentration reaches 0.1 M (Fig. 3b), demonstrating the balanced EG/OH^- adsorption and reaction capabilities. Therefore, an optimal EG concentration of 0.1 M is determined and used in the following electrochemical measurements. To verify the advantage of the EGOR over the OER, CV curves at 5 mV s^{-1} for Co-CeF_3@Ni_3N/NF in 1 M KOH with/without 0.1 M EG are obtained (Fig. 3c). Notably, in the presence of EG, the disappearance of Ni^{2+}/Ni^{3+} redox peaks and significant increase in the response current density indicate the occurrence of the EGOR after 1.30 V *vs.* RHE. In the backward scan curve, a larger reduction current is shown than in the forward scan process, revealing that the as-formed Ni^{3+} species may be spontaneously consumed during the scanning process.[51] As shown in Fig. 3d, the LSV curves of Co-CeF_3@Ni_3N/NF for the OER and EGOR processes are compared; the EGOR with Co-CeF_3@Ni_3N/NF reveals a much lower onset potential and a significantly promoted response current density, indicating that the EGOR is more kinetically and thermodynamically favorable than the OER. Therefore, the applied potentials required for the EGOR on Co-CeF_3@Ni_3N/NF are reduced by over 270 mV to achieve current densities from 200 to 600 mA cm^{-2} (Fig. 3e). Moreover, the Tafel slope for the EGOR process is significantly lower (42.6 mV dec^{-1}) than that for the OER process (146.3 mV dec^{-1}), indicating the excellent reaction activity and fast kinetics toward the EGOR (Fig. 3f). Furthermore, the electrocatalytic activity of Co-CeF_3@Ni_3N/NF can also be adjusted by controlling the coating amount of Co species (Fig. S6†), demonstrating the important role of the Co-based nanosheets in determining the EGOR activity. In a comparison, the EGOR activity and reaction kinetics of Co-CeF_3@Ni_3N/NF surpass most previously reported high-end Ni-based EGOR electrocatalysts (Table S2†).

Moreover, compared with F-$Ni(OH)_2$/NF, NiCeF precursor/NF and CeF_3@Ni_3N/NF, Co-CeF_3@Ni_3N/NF demonstrates the lowest onset potential and the most remarkable current response behaviour for the EGOR (Fig. 3g). A remarkable potential difference of 50 mV can be achieved with the presence of the surface coating and interfacial electronic interactions involving Co species. As depicted in Fig. 3h and Table S3,† the Nyquist plot of Co-CeF_3@Ni_3N/NF reveals the smallest semicircle, while the charge transfer resistance (R_{ct}) calculated from the fitted equivalent circuit is only 0.33 Ω, which is obvious lower than those of F-$Ni(OH)_2$/NF (8.02 Ω), NiCeF precursor/NF (8.63 Ω) and CeF_3@Ni_3N/NF (0.93 Ω). This result indicates that Co-CeF_3@Ni_3N/NF exhibits superior charge transfer kinetics for the EGOR process, which may due to the optimized surface adsorption capabilities. Furthermore, the electrochemical surface areas (ECSAs) of the as-prepared electrodes were

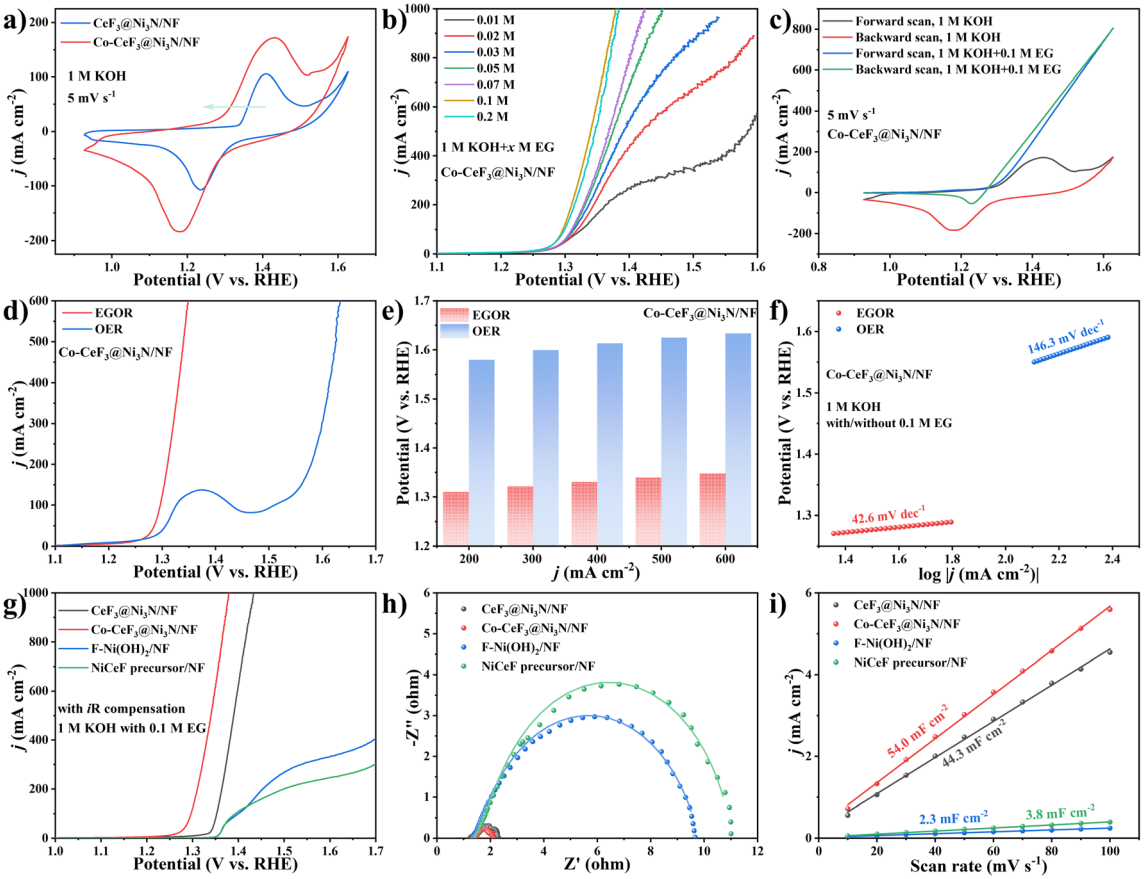

Fig. 3 (a) CV curves for Co-CeF_3@Ni_3N/NF and CeF_3@Ni_3N/NF in 1 M KOH. (b) LSV curves with varying EG concentrations for Co-CeF_3@Ni_3N/NF. (c) CV curves, (d) LSV curves, (e) potentials required for various current densities, and (f) Tafel slopes for Co-CeF_3@Ni_3N/NF for the OER and EGOR. (g) LSV curves, (h) Nyquist plots, and (i) calculated C_{dl} values for F-$Ni(OH)_2$/NF, NiCeF precursor/NF, CeF_3@Ni_3N/NF and Co-CeF_3@Ni_3N/NF for the EGOR.

assessed by measuring the double layer capacitance (C_{dl}) values (Fig. 3i and S7†). The calculated C_{dl} value of Co-CeF_3@Ni_3N/NF (54.0 mF cm^{-2}) is much higher than those of F-$Ni(OH)_2$/NF (2.3 mF cm^{-2}), NiCeF precursor/NF (3.8 mF cm^{-2}) and CeF_3@Ni_3N/NF (44.3 mF cm^{-2}), indicating the enlarged exposed surface area and active sites of the hierarchical sheet-on-sheet nanostructures for the EGOR process. Additionally, the ECSA-normalized polarization curve of Co-CeF_3@Ni_3N/NF is still lower than the other samples (Fig. S8†), indicating its superior intrinsic activity upon the introduction of Co species. Due to the high EGOR activity, the universality of Co-CeF_3@Ni_3N/NF for oxidation reactions involving other alcohols (methanol and glycerol) is evaluated. Generally, Co-CeF_3@Ni_3N/NF reveals superior oxidation activity compared with that of the OER process (Fig. S9†).

Besides the superior intrinsic activity, the durability of Co-CeF_3@Ni_3N/NF for the EGOR was investigated using chronoamperometry (*i–t*) measurements, whereas the anodic products and faradaic efficiencies (FEs) were evaluated using nuclear magnetic resonance (NMR) spectroscopy. As shown in Fig. 4a, Co-CeF_3@Ni_3N/NF underwent various *i–t* tests at intervals of 0.03 V from 1.32 to 1.44 V (*vs.* RHE). The industrial-scale response current density remains essentially stable at 1.32 V, then continuously decreases due to the rapid consumption of EG molecules with an increase in applied potential, especially at 1.44 V. Afterward, the electrolytes after *i–t* testing were examined by quantitative ^1H NMR and ^{13}C NMR. As the applied voltage increases, the EG signal located at 3.45 ppm gradually weakens (Fig. 4b), while the formate signal centred at 8.27 ppm intensifies obviously, indicating the transformation of EG to formate. Meanwhile, no CO_3^{2-} species can be detected, confirming that no inorganic carbon compounds are produced in the EGOR reaction (Fig. 4c). Moreover, the calculated FEs based on the formate product exceed 97% at the aforementioned applied potentials (Fig. 4d), demonstrating the extremely high EGOR selectivity at high current densities. To gain deeper insights into the catalytic stability and FE of Co-CeF_3@Ni_3N/NF, long-term continuous *i–t* testing for 60 h was conducted with the electrolyte refreshed every 12 h. As shown in Fig. 4e, the *i–t* curves of Co-CeF_3@Ni_3N/NF demonstrate almost consistent performance over five consecutive cycles; the immediately performance recovery after refreshing the electrolyte indicates that the decrease in response current density was mainly due to the consumption of EG. Meanwhile, the LSV curve after 60 h of testing essentially aligns well with that before *i–t* testing (inset of Fig. 4e), whereas the original sheet-on-sheet nanostructures

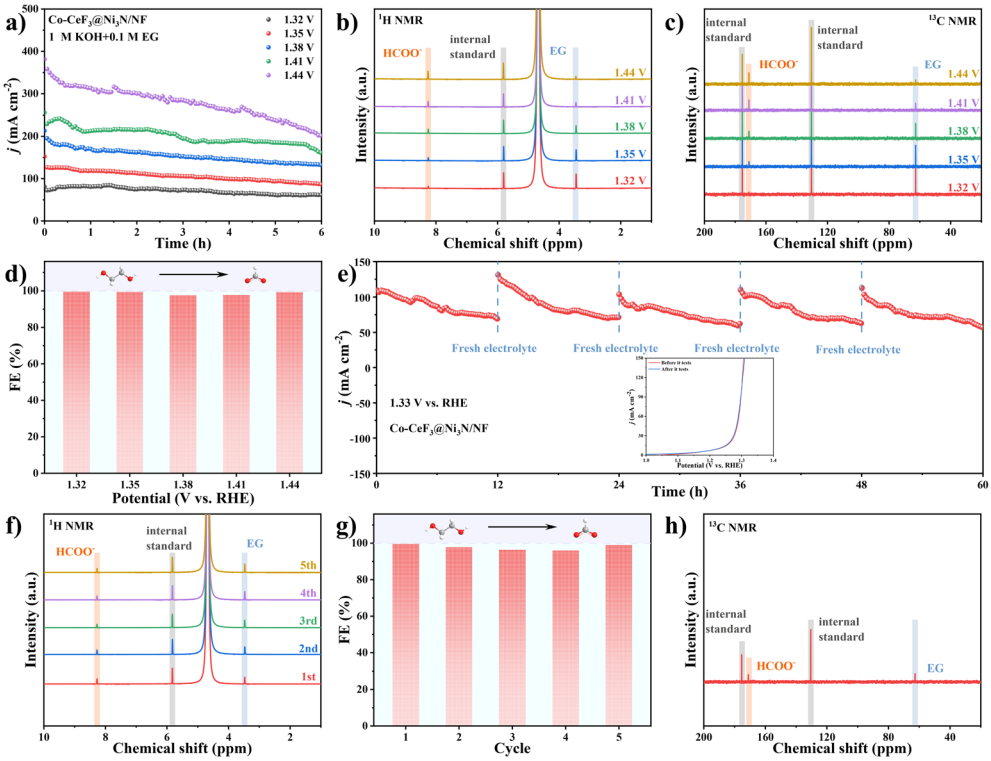

Fig. 4 (a) The *i*–*t* curves of Co-CeF_3@Ni_3N/NF at 1.32–1.44 V *vs.* RHE for 6 h, and corresponding (b) ^{1}H NMR and (c) ^{13}C NMR results from electrolytes after the EGOR. (d) Calculated formate FEs after the EG oxidation reaction. (e) The *i*–*t* curves of Co-CeF_3@Ni_3N/NF for five consecutive cycles at 1.33 V *vs.* RHE with the electrolyte refreshed every 12 h (the inset shows LSV curves before/after *i*–*t* tests). (f) Corresponding ^{1}H NMR spectra, (g) calculated formate FEs, and (h) the ^{13}C NMR spectrum for the EGOR with Co-CeF_3@Ni_3N/NF.

and the phase structure of Co-CeF_3@Ni_3N/NF show no obvious change (Fig S10–S12†). Furthermore, the anodic oxidation product of the EGOR remains solely as formate during all the long-term cycles, with formate FEs exceeding 96% (Fig. 4f–h). Therefore, Co-CeF_3@Ni_3N/NF possesses robust reaction/structural durability and excellent formate selectivity during long-term cycling for the EGOR.

Operando electrochemical impedance spectroscopy (EIS) measurements were applied at various potentials to elucidate the interfacial electrochemical behaviour of Co-CeF_3@Ni_3N/NF and CeF_3@Ni_3N/NF during the EGOR and OER. As shown in Fig. S13a,† the linear Nyquist plots of Co-CeF_3@Ni_3N/NF reveal substantial charge transfer resistance (R_{ct}) during the EGOR within the low potential range of 1.10–1.25 V *vs.* RHE. Upon increasing the applied potential to 1.30 V, the Nyquist plots undergo a notable transition from a nearly linear shape to a semicircular form. Similarly, the Nyquist plots of CeF_3@Ni_3N/NF reveal a comparable trend, with the transition to semicircular form occurring at 1.35 V (Fig. S13b†). The low-frequency region (LF) in the *operando* Bode plots is associated with charge inhomogeneity resulting from surface oxidation species, that is, the formation of oxidized species at the electrode interface.[52,53] The middle frequency (MF) corresponds to the surface double layer capacitance.[16] Co-CeF_3@Ni_3N/NF reveals a phase angle at 1.30 V *vs.* RHE in the LF region, indicating the occurrence of the EG oxidation reaction (Fig. 5a). For contrast, a similar phenomenon occurs at 1.35 V *vs.* RHE for CeF_3@Ni_3N/NF (Fig. 5b), indicating the relatively slow EGOR reaction kinetics compared to Co-CeF_3@Ni_3N/NF. For the OER process, the gradual decrease in phase angle for Co-CeF_3@Ni_3N/NF occurs at 1.50 V *vs.* RHE, indicating the initiation of oxygen evolution (Fig. S13c–f†). By fitting Nyquist plots (Fig. 5c and Table S4†), R_{ct} for the EGOR with Co-CeF_3@Ni_3N/NF reaches its lowest value at 1.30 V *vs.* RHE and then remains relatively stable. In comparison, R_{ct} for the OER also decreases to it lowest value at 1.30 V *vs.* RHE, but it subsequently exhibits a trend to slightly increase. This may be attributed to the initiation of the Ni^{2+} electro-oxidation reaction to Ni^{3+}, leading to an increase in R_{ct} values. A similar phenomenon occurs for the CeF_3@Ni_3N/NF electrode, where a comparable change can be observed at 1.35 V *vs.* RHE. The decrease of R_{ct} in CeF_3@Ni_3N/NF occurs later than that of Co-CeF_3@Ni_3N/NF, indicating inferior internal oxidation and EGOR kinetics. Therefore, Co-CeF_3@Ni_3N/NF exhibits superior adsorption capacities for OH^- and EG due to the modulated surface electronic configuration achieved through coating with Co species, which is beneficial to the accelerated EGOR.

Moreover, *in situ* Raman spectroscopy was also employed to monitor surface reconstruction and identify active phase formation for Co-CeF_3@Ni_3N/NF during EGOR and OER processes. When the applied potential exceeded 0.45 V *vs.* Ag/AgCl in the OER, two distinct peaks emerged at 465 and 540 cm^{-1} (Fig. 5d), which are attributed to Ni^{3+}–O bending (δ(Ni–O)) and Ni^{3+}–O stretching (ν(Ni–O)) vibrations, respectively.[54,55] The emergence of these two peaks indicates the

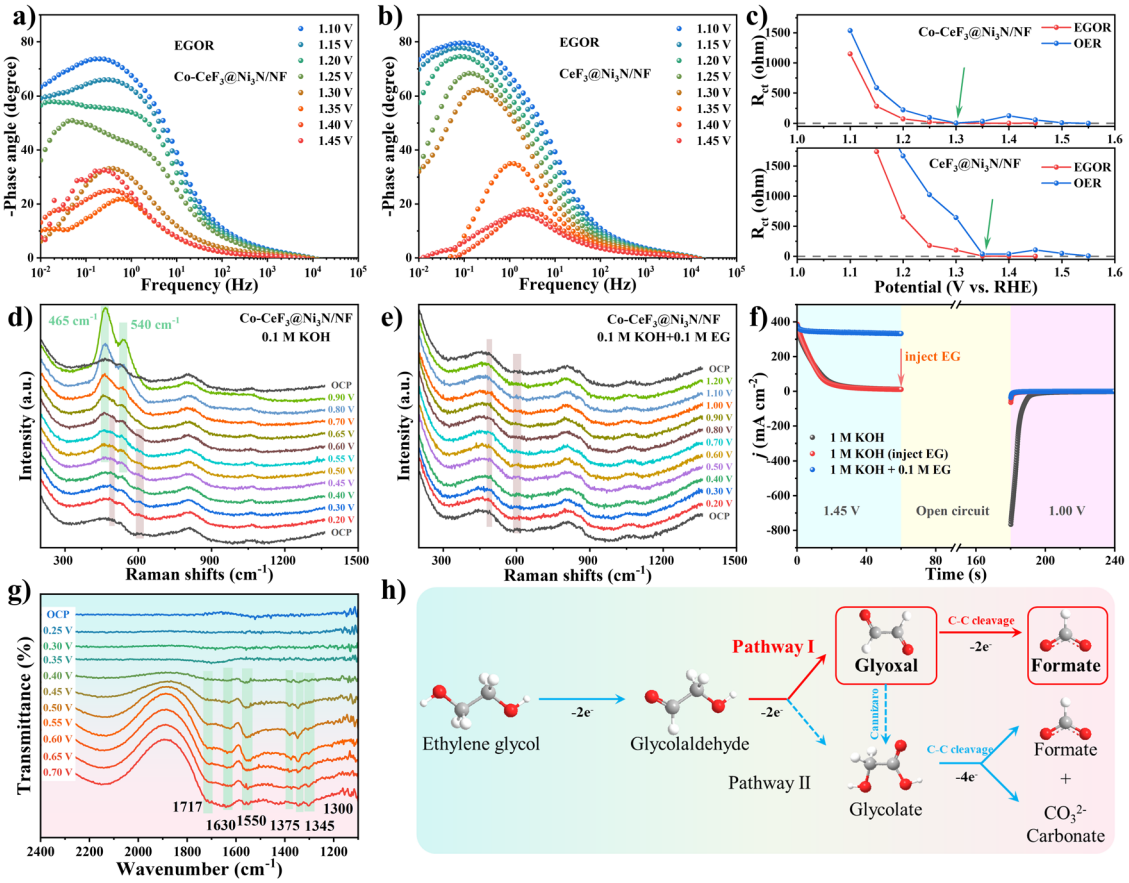

Fig. 5 *Operando* Bode plots of (a) Co-CeF_3@Ni_3N/NF and (b) CeF_3@Ni_3N/NF for the EGOR. (c) Calculated charge transfer resistance at various potentials for the OER and EGOR. *In situ* Raman spectra of Co-CeF_3@Ni_3N/NF under various applied potentials for the (d) OER and (e) EGOR. (f) Periodic electrochemical measurements for Co-CeF_3@Ni_3N/NF at 1.45 V *vs.* RHE (0–60 s), in the open circuit state (60–180 s), and at 1.00 V *vs.* RHE (180–240 s). (g) *In situ* FTIR spectra of Co-CeF_3@Ni_3N/NF at various applied potentials for the EGOR. (h) The proposed reaction pathway of the Co-CeF_3@Ni_3N/NF electrode for the electrochemical oxidation of EG to formate.

presence of high-valence $Ni^{3+}OOH$ species, which serve as the active phase during the OER process. In contrast, no obvious characteristic peaks for the $Ni^{3+}OOH$ phase can be observed in the EGOR (Fig. 5e), which may be attributed to the rapid consumption of generated $Ni^{3+}OOH$ species by EG molecules. To further prove the function of $Ni^{3+}OOH$ in the EGOR, periodic electrochemical measurements employing multiple potential steps with adjustable electrolytes are employed to separate the electrooxidation of Ni species and oxidation of EG molecules. As shown in Fig. 5f, following anodic polarization at 1.45 V *vs.* RHE for 60 s in 1 M KOH to accumulate $Ni^{3+}OOH$ species on the Co-CeF_3@Ni_3N/NF surface, the system then maintains open-circuit conditions for 120 s after injecting 0.1 M EG into the electrolyte. Subsequently, a reduction potential of 1.00 V *vs.* RHE is applied, and the reduced current density upon EG addition (red line) is clearly lower than that without the injection of EG (grey line). Similarly, no noticeable change in reduction current can be observed after switching to a reduction potential in 1 M KOH with 0.1 M EG electrolyte (blue line). Therefore, the accumulated $Ni^{3+}OOH$ species during oxidation can be rapidly and spontaneously consumed during the open-circuit process after the injection of EG, demonstrating the presence of a non-electrochemical reaction step between the $Ni^{3+}OOH$ species and EG molecules. Thus, the typical EGOR process can be divided into the electrooxidation of active sites on the electrode and the spontaneous non-electrochemical EG oxidation reaction. Moreover, the adsorption behaviour of EG at the electrode surface was evaluated through open circuit potential (OCP) measurements, providing insights into the diffusion of EG within the Helmholtz layer. As shown in Fig. S14,† upon injecting EG into KOH solution, the OCP curve of Co-CeF_3@Ni_3N/NF exhibits a more pronounced potential drop of 81 mV than that of CeF_3@Ni_3N/NF (28 mV), indicating enhanced EG adsorption kinetics and capacity within the Helmholtz layer after the coating of Co species.

To elucidate the reaction pathway and the organic intermediates of EG electrooxidation, *in situ* Fourier transform infrared (FTIR) measurements were employed on the Co-CeF_3@Ni_3N/NF electrode at different applied potentials in 1 M KOH with 1 M EG. As depicted in Fig. 5g, no distinct characteristic peaks can be observed at applied potentials below 0.35 V *vs.* Hg/HgO. When the applied potential reaches and exceeds 0.40 V *vs.* Hg/HgO, several new peaks emerge in the range of 1300–1400 cm^{-1}, which are consistent with the O–C–O symmetric stretching vibrations of carboxylate.[56] Additionally, the signal located at 1550 cm^{-1} belongs to the O–C–O antisymmetric stretching

vibrations of carboxylate,[57,58] indicating the generation of formate. The small peak centred at 1717 cm^{-1} is attributed to the presence of aldehyde intermediates, possibly related to glyoxal molecules.[32] However, according to the FTIR spectra, it is difficult to precisely determine the presence of other intermediates. Therefore, the electrooxidation behaviour of the possible key intermediates, glycolic acid (GA) and oxalic acid (OA), was evaluated by the addition of each molecule at 0.1 M into 1 M KOH electrolyte to further understand their reaction activities and subsequent pathways. Fig. S15a† presents the LSV curves of EG, GA, and OA oxidation reactions, respectively, using the Co-CeF_3@Ni_3N/NF electrode. Obviously, the electrocatalytic activities of EG and GA are significantly higher than that of OA, implying that OA is probably not an intermediate in the EGOR reaction pathway. To further elucidate the anodic oxidation products of GA, the electrolyte was analyzed by ^{13}C NMR and ^{1}H NMR spectroscopy after 3 h of *i–t* testing (Fig. S15b†). As depicted in Fig. S15c,† both formate and carbonate can be detected, and the intensities of their characteristic peaks are almost identical in ^{13}C NMR, indicating that GA can be oxidized to yield approximately equal amounts of formate and carbonate molecules. Therefore, a possible pathway for GA oxidation on the Co-CeF_3@Ni_3N/NF electrode is proposed in Fig. S15d.† In addition to formate, the substantial presence of carbonate species in the anodic oxidation products of GA implies that GA is likely not an intermediate during the EGOR process. Thus, by referring to the relevant literature and the above results, the EGOR process on the Co-CeF_3@Ni_3N/NF electrode likely follows pathway I illustrated in Fig. 5h, and glyoxal serves as a crucial reaction intermediate. In brief, ethylene glycol is initially oxidized to glycolaldehyde, which is then further oxidized to glyoxal. By the electrochemical cleavage of the C–C bond, the glyoxal molecule is finally converted to two molecules of formate.

Furthermore, the HER performance of the Co-CeF_3@Ni_3N/NF electrocatalyst was also measured to evaluate its multifunctionality. As shown in Fig. S16a and b,† compared with the comparison electrodes, Co-CeF_3@Ni_3N/NF reveals exceptional HER performance, with overpotentials of only 50 and 70 mV to achieve 50 and 100 mA cm^{-2}, respectively. Moreover, the Tafel slope of Co-CeF_3@Ni_3N/NF (64.4 mV dec^{-1}) further confirms its superior intrinsic activity (Fig. S16c†), which is lower than those of F-$Ni(OH)_2$/NF (123.5 mV dec^{-1}), NiCeF precursor/NF (118.8 mV dec^{-1}), and CeF_3@Ni_3N/NF (67.0 mV dec^{-1}). Furthermore, the Nyquist plots and calculated resistance values of Co-CeF_3@Ni_3N/NF underscore the significantly lower R_{ct} values, indicating superior charge transfer efficiency due to the interfacial electronic interactions between heteroatoms (Fig. S16d and Table S5†). Meanwhile, the durability of Co-CeF_3@Ni_3N/NF was evaluated at 100 mA cm^{-2} for 30 h (Fig. S16e†). The applied potential essentially levels off, suggesting the highly stable HER activity of Co-CeF_3@Ni_3N/NF. As the HER performance of Co-CeF_3@Ni_3N/NF can surpass most reported high-end HER catalysts (Fig. S16f and Table S6†), it possesses promising potential as a bifunctional electrocatalyst for the HER and EGOR.

With a comprehensive understanding of the specific active sites and the EG electrooxidation mechanism of Co-CeF_3@Ni_3N/NF, we are dedicated to exploring the practical upgrading of real PET plastic waste. Firstly, the PET raw materials were hydrolyzed in KOH solution at 180 °C for 12 h to achieve high yields of monomeric EG and TPA. The formation of EG and TPA molecules was confirmed by ^{1}H NMR and ^{13}C NMR spectra (Fig. S17†), and the PET hydrolysate is directly diluted to form the electrolyte (please see the ESI for detailed information†). Fig. 6a shows the LSV curves of Co-CeF_3@Ni_3N/NF and CeF_3@Ni_3N/NF in the presence of PET hydrolysate. Compared to CeF_3@Ni_3N/NF, the electrooxidation activity toward the PET hydrolysate of Co-CeF_3@Ni_3N/NF is significantly enhanced: the anodic potential difference is approximately 65 mV at 100 mA cm^{-2}. This indicates that the incorporation of Co species into Co-CeF_3@Ni_3N/NF effectively enhances the EGOR performance. Moreover, formate was identified as the sole anodic oxidation product, with the FE reaching up to 99.34% for a 6-h electrolysis process (Fig. 6b and S18†). Motivated by the superior intrinsic electrocatalytic activity of Co-CeF_3@Ni_3N/NF for both the HER and EGOR, a continuous co-electrolysis flow reactor was constructed using Co-CeF_3@Ni_3N/NF as both the anode and cathode for electro-upgrading PET hydrolysate, coupled with hydrogen production (Fig. 6c). The flow reactor requires a cell potential of only 1.50 V to achieve a response current density of 100 mA cm^{-2}, while a much higher applied potential of 1.72 V is necessary for traditional overall water splitting systems (Fig. 6d). A substantial voltage reduction of 217 mV (at 100 mA cm^{-2}) can be achieved when utilizing the PET hydrolysate electro-upgrading system, which is beneficial for both electronic power costs (12.6% lower) and the value promotion of products. Meanwhile, the theoretical energy consumption to produce 1 kg/1 Nm^3 of hydrogen is estimated to be 40.20/3.59 kW h when operated at 100 mA cm^{-2}.[59] To evaluate the stability and FEs of the reaction system, long-term *i–t* testing was conducted at 1.75 V for 144 h with the electrolyte being refreshed every 24 h. As illustrated in Fig. 6e, the *i–t* curves of the flow reactor exhibit consistent performance over six consecutive cycles, while the gradually decreased response current density is mainly due to the consumption of EG molecules. Moreover, the industrial-scale response current density can be maintained at over 120 mA cm^{-2} during the entire 144 h of testing, demonstrating fast and balanced surface adsorption kinetics for OH^-/EG reactants. Additionally, the LSV curve obtained after stability testing aligns well with that before testing (Fig. S19†), indicating the satisfied catalytic stability of Co-CeF_3@Ni_3N/NF as a bifunctional electrocatalyst. Furthermore, formate is identified as the predominant product in the electrolyte (Fig. S20†), and the calculated formate FEs remain over 96% for consecutive cycles (Fig. 6f), surpassing most bifunctional electrocatalysts in PET hydrolysates (Table S7†). After electrolysis, the electrolyte can be acidified using H_2SO_4 to extract pure TPA powder (Fig. 6g), as confirmed by XRD characterization (Fig. S21†), highlighting the good molecular preservation of the TPA monomers during the long-term electrocatalytic upgrading of PET hydrolysate. Moreover, related FA and K_2SO_4 products can be collected by a series of condensation, purification and recrystallization processes.[60,61] Overall, the electro-upgrading of PET hydrolysate in the Co-CeF_3@Ni_3N/NF‖Co-CeF_3@Ni_3N/NF co-electrolysis system is not only energy

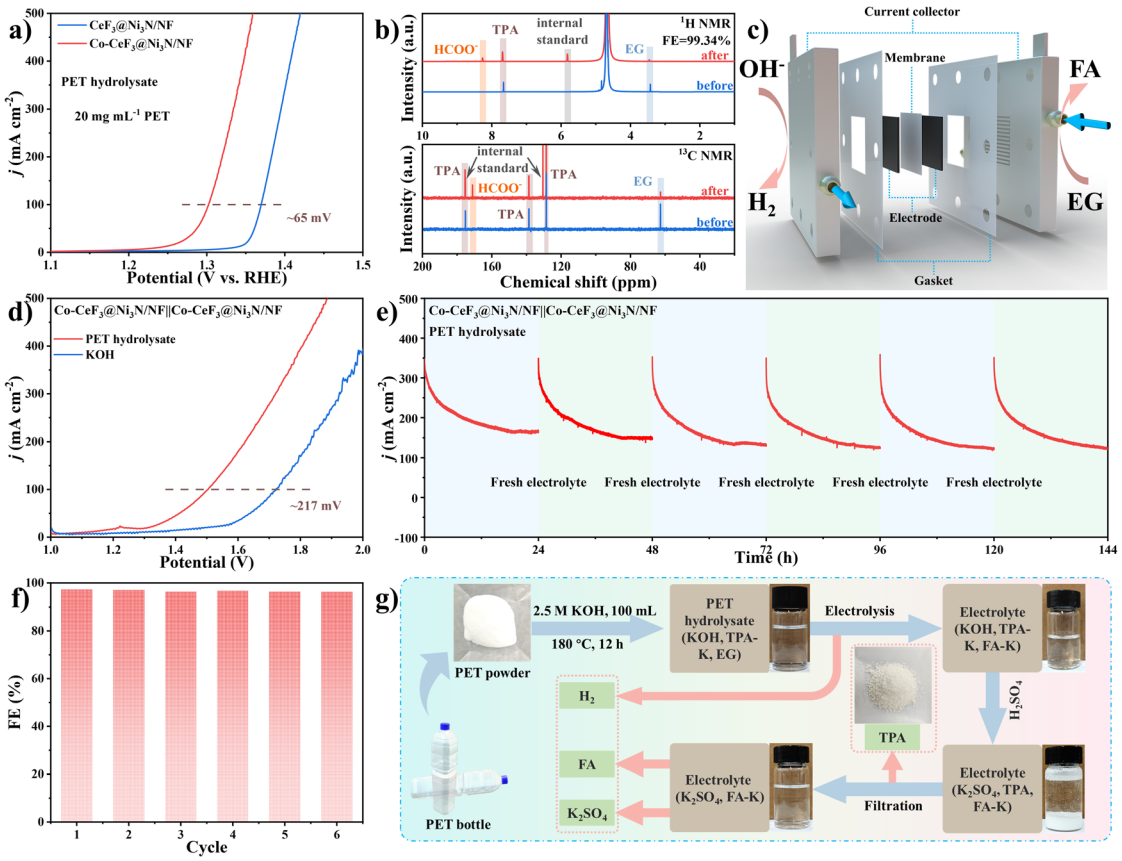

Fig. 6 (a) LSV curves of Co-CeF_3@Ni_3N/NF and CeF_3@Ni_3N/NF in PET hydrolysate, and related (b) ^{1}H NMR and ^{13}C NMR spectra of PET hydrolysate before/after electrooxidation. (c) A schematic diagram of a continuous two-electrode flow cell system for PET hydrolysate upgrading coupled with hydrogen production. (d) LSV curves of the Co-CeF_3@Ni_3N/NF||Co-CeF_3@Ni_3N/NF system in PET hydrolysate. (e) Long-term *i*–*t* curves for the continuous flow cell in PET hydrolysate, and (f) corresponding formate FEs after each *i*–*t* cycle. (g) A schematic illustration of the electro-upgrading route for transforming PET waste into TPA and FA.

efficient and economically viable but also promotes the cost-effective and closed-loop utilization of PET plastic waste.

Conclusions

In summary, hierarchical Co-CeF_3@Ni_3N sheet-on-sheet nanostructures supported on nickel foam were fabricated, which can be utilized as a bifunctional electrocatalyst for the electro-upgrading of PET hydrolysate towards energy-effective hydrogen and value-added product production. The rational modulation of the electronic configuration through the introduction of Co species can optimize the adsorption kinetics/behaviour of the key reactants and intermediates, as well as decrease the oxidation potential of Ni^{3+}OOH, thereby enhancing both the electrocatalytic activity and selectivity of the EGOR. Therefore, Co-CeF_3@Ni_3N/NF exhibits industrial-scale response current densities of around 80–380 mA cm^{-2}, along with high stability over 60 h and high formate FEs of over 97% at around 1.32–1.44 V *vs.* RHE. Moreover, Co-CeF_3@Ni_3N/NF reveals high HER activity with an overpotential of only 50 mV to achieve 50 mA cm^{-2}. A continuous flow reactor using Co-CeF_3@Ni_3N/NF as the bifunctional electrocatalyst and PET hydrolysate as the electrolyte delivers excellent electrocatalytic activity (1.72 V@300 mA cm^{-2}), long-term stability (144 h) and FEs (over 95%). Based on *in situ* characterization and various electrochemical measurements, the key active centres and a possible reaction pathway for the EGOR are elucidated. This study successfully develops an excellent electrocatalyst for the EGOR coupled with hydrogen production, emphasizing the important role of reactant/intermediate adsorption on active sites for obtaining high-selectivity and closed-loop chemical utilization for PET waste upgrading.

Data availability

The data that support the findings of this study are available from the corresponding author, Junyi Ji, upon reasonable request.

Author contributions

K. D.: conceptualization, investigation, data collection, writing – original draft; X. L.: data collection, investigation; P. L.: software, validation; X. L.: software, visualization; W. T.: methodology, writing – review & editing; J. J.: conceptualization, funding acquisition, supervision, writing – review & editing.

Conflicts of interest

There are no conflicts to declare.

Acknowledgements

This work was financially supported by National Natural Science Foundation of China (22278282), and Sichuan Science and Technology Program (2023NSFSC1915, 2024NSFSC1137). We would like to thank Yanping Huang and Wen Tian from Center of Engineering Experimental Teaching for the help with SEM, NMR and FTIR measurements, and Yingming Zhu from the Institute of New Energy and Low Carbon Technology for XRD and Raman analysis.

Notes and references

1 A. Rahimi and J. M. García, *Nat. Rev. Chem.*, 2017, **1**, 0046.
2 H. Zhou, Y. Wang, Y. Ren, Z. Li, X. Kong, M. Shao and H. Duan, *ACS Catal.*, 2022, **12**, 9307–9324.
3 A. Stubbins, K. L. Law, S. E. Muñoz, T. S. Bianchi and L. Zhu, *Science*, 2021, **373**, 51–55.
4 Y. Li, L. Q. Lee, H. Zhao, Y. Zhao, P. Gao and H. Li, *J. Mater. Chem. A*, 2024, **12**, 2121–2128.
5 F. Ma, C. Zhang, W. Li, R. Hu, Z. Wang, J. Wang, J. Li, Y. Nie, Z. Zheng and X. Jiang, *ACS Catal.*, 2025, **15**, 4759–4769.
6 C. He, Y. Yan, Y. Fu, C. Ma, J. Xia, S. Han, H. Zhang, X. Ma, G. Lin, F. Feng, X. Meng, W. Cao, L. Zhu, Z. Li and Q. Lu, *Adv. Mater.*, 2025, 2418959.
7 J. Qi, Y. Xia, X. Meng, J. Li, S. Yang, H. Zou, Y. Ma, Y. Zhang, Y. Du, L. Zhang, Z. Lin and J. Qiu, *Adv. Mater.*, 2025, **37**, 2419058.
8 C. V. Aarsen, A. Liguori, R. Mattsson, M. H. Sipponen and M. Hakkarainen, *Chem. Rev.*, 2024, **124**, 8473–8515.
9 V. Tournier, C. M. Topham, A. Gilles, B. David, C. Folgoas, E. Moya-Leclair, E. Kamionka, M. L. Desrousseaux, H. Texier, S. Gavalda, M. Cot, E. Guémard, M. Dalibey, J. Nomme, G. Cioci, S. Barbe, M. Chateau, I. André, S. Duquesne and A. Marty, *Nature*, 2020, **580**, 216–219.
10 S. Behera, S. Dinda, R. Saha and B. Mondal, *ACS Catal.*, 2023, **13**, 469–474.
11 J. Chen, M. Jiang, F. Zhang, L. Wang and J. Yang, *Adv. Mater.*, 2024, **36**, 2401867.
12 F. Ma, S. Wang, X. Gong, X. Liu, Z. Wang, P. Wang, Y. Liu, H. Cheng, Y. Dai, Z. Zheng and B. Huang, *Appl. Catal., B*, 2022, **307**, 121198.
13 X.-H. Wang, Z.-N. Zhang, Z. Wang, Y. Ding, Q.-G. Zhai, Y.-C. Jiang, S.-N. Li and Y. Chen, *Chem. Eng. J.*, 2023, **465**, 142938.
14 X. Liu, X. He, D. Xiong, G. Wang, Z. Tu, D. Wu, J. Wang, J. Gu and Z. Chen, *ACS Catal.*, 2024, **14**, 5366–5376.
15 L. Wu, Q. Wu, Y. Han, D. Zhang, R. Zhang, N. Song, X. Wu, J. Zeng, P. Yuan, J. Chen, A. Du, K. Huang and X. Yao, *Adv. Mater.*, 2024, **36**, 2401857.
16 J. Wu, J. Chen, T. Yu, Z. Zhai, Y. Zhu, X. Wu and S. Yin, *ACS Catal.*, 2023, **13**, 13257–13266.
17 H. Tian, X. Wang, W. Luo, R. Ma, X. Yu, S. Li, F. Kong, X. Cui and J. Shi, *Chem. Sci.*, 2024, **15**, 11013–11020.
18 G. Zhao, J. Lin, M. Lu, L. Li, P. Xu, X. Liu and L. Chen, *Nat. Commun.*, 2024, **15**, 8463.
19 K. Liu, X. Gao, C.-X. Liu, R. Shi, E. C. M. Tse, F. Liu and Y. Chen, *Adv. Energy Mater.*, 2024, **14**, 2304065.
20 J. Qi, Y. Du, Q. Yang, N. Jiang, J. Li, Y. Ma, Y. Ma, X. Zhao and J. Qiu, *Nat. Commun.*, 2023, **14**, 6263.
21 Y. Luo, Z. Zhang, M. Chhowalla and B. Liu, *Adv. Mater.*, 2022, **34**, 2108133.
22 H. Zhang, Z. Liu, H. Li, Z. Fu, G. Zhang, H. Zhang, G. Wang and Y. Zhang, *J. Mater. Chem. A*, 2024, **12**, 15984–15995.
23 L. Sun, H. Lv, J. Xiao and B. Liu, *Adv. Mater.*, 2024, **36**, 2402767.
24 Y. Wang, K. Liu, F. Liu, C. Liu, R. Shi and Y. Chen, *Green Chem.*, 2023, **25**, 5872–5877.
25 J. Zhang, X. Zhang, C. Shi, X. Yu, Y. Zhou and L. Di, *Small*, 2024, **20**, 2406767.
26 Y. Lin, Y. Chen, H. Ren, Y. Sun, J. Chen, M. Wu and Z. Li, *Adv. Funct. Mater.*, 2024, **34**, 2404594.
27 Y. Du, X. Meng, Y. Ma, J. Qi, G. Xu, H. Zou and J. Qiu, *Adv. Funct. Mater.*, 2024, **34**, 2408013.
28 T. Zhang, X. Li, J. Wang, Y. Miao, T. Wang, X. Qian and Y. Zhao, *J. Hazard. Mater.*, 2023, **450**, 131054.
29 Y. Yan, H. Zhou, S.-M. Xu, J. Yang, P. Hao, X. Cai, Y. Ren, M. Xu, X. Kong, M. Shao, Z. Li and H. Duan, *J. Am. Chem. Soc.*, 2023, **145**, 6144–6155.
30 Y. Li, X. Wei, R. Pan, Y. Wang, J. Luo, L. Li, L. Chen and J. Shi, *Energy Environ. Sci.*, 2024, **17**, 4205–4215.
31 C.-A. Zhou, S. Wang, K. Ma, L. Song, L. Zheng and H. Yue, *Appl. Catal., B*, 2023, **321**, 122065.
32 Z. Wang, J. Li, Q. Zhang, C. Wu, H. Meng, Y. Tang, A. Zou, Y. Zhang, R. Ma, X. Lv, Z. Yu, S. Xi, J. Xue, X. Wang and J. Wu, *Angew. Chem., Int. Ed.*, 2024, **63**, e202411517.
33 J. Wang, X. Li, T. Zhang, Y. Chen, T. Wang and Y. Zhao, *J. Phys. Chem. Lett.*, 2022, **13**, 622–627.
34 Z. Zhao, X. Shen, X. Luo, M. Chen, M. Zhang, R. Yu, R. Jin and H. Zheng, *Adv. Energy Mater.*, 2024, **14**, 2400851.
35 Y. Feng, R. L. Smith, J. Fu and X. Qi, *Green Chem.*, 2023, **25**, 8698–8705.
36 K. Deng, X. Liu, P. Liu, X. Lv, W. Tian and J. Ji, *Angew. Chem., Int. Ed.*, 2025, **64**, e202416763.
37 T. Wu, E. Song, S. Zhang, M. Luo, C. Zhao, W. Zhao, J. Liu and F. Huang, *Adv. Mater.*, 2021, **24**, 2108505.
38 Y. Dong, Y. Wu, X. Wang, H. Wang, J. Ren, P. Wang, L. Pan, G. Wang and R. Wang, *Nanoscale*, 2023, **15**, 1813–1823.
39 Y. Ma, X. Meng, K. Li, L. Zhang, Y. Du, X. Cai and J. Qiu, *ACS Catal.*, 2023, **13**, 1290–1298.
40 F. Zhang, Y. Liu, F. Yu, H. Pang, X. Zhou, D. Li, W. Ma, Q. Zhou, Y. Mo and H. Zhou, *ACS Nano*, 2023, **17**, 1681–1692.
41 M. Li, X. Wu, K. Liu, Y. Zhang, X. Jiang, D. Sun, Y. Tang, K. Huang and G. Fu, *J. Energy Chem.*, 2022, **69**, 506–515.
42 W. Sha, Y. Song, P. Liu, J. Wang, B. Xu, X. Feng and J. Guo, *ChemCatChem*, 2022, **14**, e202101975.
43 X. Zhang, X. Wang, Q. Yan, R. Gao, J. Zhao, Z. Song, K. Zhu, D. Cao, J. Yao, L. Zheng and G. Wang, *Chem. Eng. J.*, 2024, **486**, 150397.

44 B. Singh, T. Ansari, N. Verma, Y.-C. Huang, P. Mannu, C.-L. Dong and A. Indra, *J. Mater. Chem. A*, 2024, **12**, 19321–19330.
45 T. Ren, Z. Duan, H. Wang, H. Yu, K. Deng, Z. Wang, H. Wang, L. Wang and Y. Xu, *ACS Catal.*, 2023, **13**, 10394–10404.
46 J. Li, X. Meng, X. Song, J. Qi, F. Liu, X. Xiao, Y. Du, G. Xu, Z. Jiang, S. Ye, S. Huang and J. Qiu, *Adv. Funct. Mater.*, 2024, **34**, 2316718.
47 R. Liu, M. Sun, X. Liu, Z. Lv, X. Yu, J. Wang, Y. Liu, L. Li, X. Feng, W. Yang, B. Huang and B. Wang, *Angew. Chem., Int. Ed.*, 2023, **62**, e202312644.
48 S. Yang, X. Xiang, Z. He, W. Zhong, C. Jia, Z. Gong, N. Zhang, S. Zhao and Y. Chen, *Chem. Eng. J.*, 2023, **457**, 141344.
49 P. Li, S. Zhao, Y. Huang, Q. Huang, Y. Yang and H. Yang, *ACS Catal.*, 2023, **13**, 15360–15374.
50 G. Liu, T. Nie, Z. Song, X. Sun, T. Shen, S. Bai, L. Zheng and Y.-F. Song, *Angew. Chem., Int. Ed.*, 2023, **62**, e202311696.
51 J. Wang, X. Li, T. Zhang, X. Chai, M. Xu, M. Feng, C. Cai, Z. Chen, X. Qian and Y. Zhao, *Chem. Sci.*, 2024, **15**, 7596–7602.
52 Y. Qi, Y. Zhang, L. Yang, Y. Zhao, Y. Zhu, H. Jiang and C. Li, *Nat. Commun.*, 2022, **13**, 4602.
53 H.-Y. Wang, S.-F. Hung, H.-Y. Chen, T.-S. Chan, H. M. Chen and B. Liu, *J. Am. Chem. Soc.*, 2016, **138**, 36–39.
54 H. Zhang, Q. Yang, S. Luo, Z. Liu, J. Huang, Y. Zheng, C. Hu, J. Zhang, X. Bao, P. Yuan and X. Yao, *ACS Catal.*, 2024, **14**, 9565–9574.
55 Y.-N. Zhou, F.-T. Li, B. Dong and Y.-M. Chai, *Energy Environ. Sci.*, 2024, **17**, 1468–1481.
56 X. Liu, Z. Fang, D. Xiong, S. Gong, Y. Niu, W. Chen and Z. Chen, *Nano Res.*, 2022, **16**, 4625–4633.
57 S. He, Y. Liu, H. Li, Q. Wu, D. Ma, D. Gao, J. Bi, Y. Yang and C. Cui, *ACS Appl. Mater. Interfaces*, 2021, **13**, 13311–13318.
58 J. Li, L. Li, X. Ma, X. Han, C. Xing, X. Qi, R. He, J. Arbiol, H. Pan, J. Zhao, J. Deng, Y. Zhang, Y. Yang and A. Cabot, *Adv. Sci.*, 2023, **10**, 2300841.
59 X. Liu, H. Qin, G. Wang, Q. Li, Q. Huang, Z. Wen and S. Mao, *J. Mater. Chem. A*, 2022, **10**, 16825–16833.
60 F. Liu, X. Gao, R. Shi, E. C. M. Tse and Y. Chen, *Green Chem.*, 2022, **24**, 6571–6577.
61 H. Zhou, Y. Ren, Z. Li, M. Xu, Y. Wang, R. Ge, X. Kong, L. Zheng and H. Duan, *Nat. Commun.*, 2021, **12**, 4679.